

Frequency-dependent complex viscosity obtained for a liquid two-dimensional dusty plasma experiment

Jorge Berumen  and J. Goree 

Department of Physics and Astronomy, University of Iowa, Iowa City, Iowa 52242, USA



(Received 30 August 2021; accepted 7 January 2022; published 28 January 2022)

Strongly coupled plasmas in a liquid phase can be characterized by a complex viscosity $\eta(\omega)$, which is a function of frequency. Data from a single experiment with dusty plasma were analyzed to compare $\eta(\omega)$ obtained by two fundamentally distinct methods. In a nonequilibrium method, a pair of counterpropagating laser beams, separated by a gap, applied a sinusoidal shear to a two-dimensional liquid, and $\eta(\omega)$ was determined using the constitutive relation. In an equilibrium method, there was no externally applied shear, so $\eta(\omega)$ could be calculated with a generalized Green-Kubo relation. The results for these two methods are compared for the real and imaginary parts of $\eta(\omega)$. For both parts, it is confirmed that the two methods yield results that agree qualitatively in their trends with frequency, with the real part diminishing with ω and the imaginary part increasing with ω , as expected for viscoelastic liquids. Quantitatively, the values of $\eta(\omega)$ obtained by the two methods differ slightly. For the experiment that we analyze, values for the real and imaginary parts of $\eta(\omega)$ are substantially greater than those reported in an earlier experiment, which we attribute to shear thinning effects in the earlier experiment. The experiment we analyze was designed to minimize shear thinning, unlike the earlier experiment.

DOI: [10.1103/PhysRevE.105.015209](https://doi.org/10.1103/PhysRevE.105.015209)

I. INTRODUCTION

Soft materials, including liquids, can exhibit viscoelasticity when subjected to a time-dependent deformation [1]. For deformations with short timescales, the material's behavior is mostly elastic, with a *storage* of energy. On the other hand, at long timescales, the behavior is mostly viscous, with a *dissipation* of energy in the form of heat. This viscous dissipation of energy is connected to a microscopic rearrangement of nearest neighbors.

The liquid phase of matter of interest for this paper is that of a strongly coupled plasma. For a strongly coupled plasma, relaxation processes that are typical of viscoelastic behavior were already an established research topic when Ichimaru wrote a landmark review paper in 1982 [2]. Viscoelastic behavior was subsequently studied using theories [3–17], simulations [13,18,19], and experiments [20–25].

A strongly coupled plasma is a collection of charged particles, with an interparticle potential energy greater than their thermal kinetic energy. This condition can be expressed as an inequality $\Gamma > 1$, where the Coulomb coupling parameter is

$$\Gamma = \frac{Q^2}{4\pi\epsilon_0 a_{\text{ws}} k_B T_k}. \quad (1)$$

For liquid conditions, Γ is typically of order 10^2 . In Eq. (1), Q is the charge of an individual particle, T_k is the kinetic temperature of the particles, and a_{ws} is the Wigner-Seitz radius, which is a measure of interparticle distances. Some examples of strongly coupled plasmas are non-neutral ion plasmas [26], ultracold plasmas [27,28], and dusty plasmas [29].

A dusty plasma is a mixture of four components: ions, electrons, neutral gas, and dust particles, which are small particles of solid matter. For micron-sized particles, a large negative charge of thousands of elementary charges accumulates on the dust particle. With this large charge, it is easy to attain a large value of Γ , and for this reason the dust component tends to be strongly coupled in a dusty plasma [30–34].

Dusty plasma experiments are often performed in either solid [35–37] or liquid states [24,25,38–43]. In experiments, liquids can be prepared by first forming a crystal and then melting it using laser heating [41,44,45], which exploits radiation pressure forces [46,47]. The laser heating, along with heating due to ion flow, provides an energy input to the dust component, which is balanced by frictional cooling on the neutral gas. The microscopic motion of the dust particles can mimic that of atoms in a liquid under thermal equilibrium [41,44], even though the collection of particles is not truly in equilibrium because of the external energy input by lasers and ions and the external cooling by neutral gas. Many of these liquidlike dusty plasma experiments were performed with a two-dimensional dust cloud, electrically levitated by a strong vertical electrical field and confined at the boundaries by a weaker horizontal field.

Numerical simulations of strongly coupled dusty plasmas are often performed using molecular-dynamics methods, tracking individual particles that are assumed to interact by a shielded Coulomb repulsive potential [48]. These simulations often show good agreement with experiments [49] although they are greatly simplified, neglecting effects present in experiments, such as ion heating and gradients arising from external confinement.

A common description of viscoelastic properties, for all kinds of substances, is a frequency-dependent *complex* viscosity [1,50–52]

$$\eta(\omega) = \eta'(\omega) - i\eta''(\omega), \quad (2)$$

where the real part $\eta'(\omega)$ represents the viscous response of the substance and the imaginary part $\eta''(\omega)$ represents the elastic response. The variable ω captures the timescale. In the zero-frequency limit, there is the familiar static viscosity $\eta^0 \equiv \eta'(0)$. As an alternative to Eq. (2), viscoelasticity is described by some authors [1,51,53] by a complex modulus $G(\omega)$.

Two common methods for obtaining the complex viscosity of a liquid are what we will call the nonequilibrium and equilibrium methods.

The *nonequilibrium* method is based on a constitutive relation [54], which is a ratio of the flux of momentum, the shear stress P_{xy} , and the gradient of flow velocity, the shear rate γ . This method requires an external source to sustain the macroscopic gradient in velocity, which makes this physical system intrinsically nonequilibrium. For soft materials, other than dusty plasmas, rheometers are used to measure the complex viscosity using the nonequilibrium method by applying an external stress at a specified frequency [1,53,55,56].

The *equilibrium* method is based on a generalized Green-Kubo relation [57–60]. The complex viscosity is obtained by using the microscopic fluctuations of particle positions, velocities, and potentials to obtain the shear stress P_{xy} . Integrating the shear-stress autocorrelation yields $\eta(\omega)$. This method assumes thermal conditions, with no macroscopic gradients, and for that reason we term it an equilibrium method. The equilibrium method is most commonly used for simulations that capture the microscopic motion of individual particles, which is possible in only a few kinds of experiments, such as dusty plasmas.

For liquidlike dusty plasmas, the two methods described above have been used in previous studies of viscoelastic properties. Experiments were performed in two-dimensional liquid dusty plasmas by Hartmann *et al.* [24], who only used the nonequilibrium method, and Feng *et al.* [25], who only used the equilibrium method. Simulations have been reported by Kovács *et al.* [61], using only the nonequilibrium method for a 2D liquid, and by Donkó *et al.* [18], using both methods in a 3D liquid. For the Kovács *et al.* 2D simulations, the effects of shear thinning on the frequency-dependent complex viscosity were characterized as well. For the Donkó *et al.* 3D simulations, the two methods were compared, and found to agree within a few percent, under conditions that were as alike as practical. The simulation results of Kovács *et al.* and Donkó *et al.* motivate our experimental effort to make a comparison between both methods for calculating the frequency-dependent complex viscosity, while minimizing shear thinning effects. For the static viscosity η^0 , on the other hand, the experiment of Haralson and Goree [42] compared the two methods, using separate runs with and without external shear in the same experiment. Their results for η^0 , for the two methods, were generally comparable, but with a quantitative difference of about 60%.

In this paper, we analyze data from our previously reported experiment [43] to obtain a frequency-dependent complex

viscosity. Here we perform a different analysis of these data. The physical concept studied in Ref. [43] was the hydrodynamics phenomenon of a Stokes layer, which is a *macroscopic flow pattern*. Here, instead of a flow pattern, our focus is a *material property*, the complex viscosity $\eta(\omega)$. Our study of $\eta(\omega)$ involves not only macroscopic measurements but also microscopic measurements of the shear stress. We analyze separate runs from the experiment, with and without external shear, to obtain $\eta(\omega)$ using the nonequilibrium and equilibrium methods, respectively. The shear was provided by a pair of laser beams separate from those used for heating the cloud and sustaining liquid conditions.

We make a quantitative comparison between our nonequilibrium method results and those reported for an earlier experiment by Hartmann *et al.* [24]. We find that there is a significant difference between our complex viscosity values and those obtained by Hartmann *et al.*, which we attribute to shear thinning effects in the earlier experiment.

We find that the equilibrium and nonequilibrium methods agree qualitatively in the 2D experiment we analyze [43], but their quantitative difference is greater than for the 3D simulations of Donkó *et al.* [18]. Some possible reasons for this discrepancy between experiments and simulations are discussed as well.

Aside from our results for the time-dependent phenomenon of viscoelasticity, we also obtain results for static viscosity, which are consistent with the previous experiment of Haralson and Goree [42].

II. PHYSICAL QUANTITIES FOR THE 2D DUSTY PLASMA LIQUID

Relevant formulas for obtaining the shear stress and shear rate are listed here. We begin with the length and timescales used to normalize our results into dimensionless quantities. Then we list the notation and formulas for velocities, shear rate γ , and shear stress P_{xy} , which will all be used in Sec. III to obtain the frequency-dependent complex viscosity.

A. Normalization

Two length scales of interest are the Wigner-Seitz radius and the screening length. The Wigner-Seitz radius $a_{ws} = (\pi n)^{-1/2}$ characterizes the interparticle spacing in a liquid with particle areal density n . The screening length λ_D describes the shielding of a dust particle’s electric charge due to the space charge of ions and electrons near the dust particle. Combining these two length scales yields the screening parameter $\kappa = a_{ws}/\lambda_D$.

The microscopic timescale for collective particle motion is characterized by the nominal 2D dust plasma frequency $\omega_{pd} = (Q^2/2\pi\epsilon_0 m_d a_{ws}^3)^{1/2}$. Here, m_d is the mass of a dust particle.

A characteristic value of viscosity can be defined by dimensional analysis as the product $\rho a_{ws}^2 \omega_{pd}$. This value will be used for normalizing our results. Here, $\rho = nm_d$ is the areal mass density of the dust particle cloud.

B. Velocities

We present here our notation for velocities in both the particle and hydrodynamic paradigms. In the particle paradigm,

for a particle i with position $\mathbf{r}_i(t) = (x_i(t), y_i(t))$, we have the time-resolved velocity $\mathbf{v}_i(\mathbf{r}_i, t) = (v_{ix}(\mathbf{r}_i, t), v_{iy}(\mathbf{r}_i, t))$. Both these vector quantities can be obtained experimentally using particle tracking velocimetry. The particle velocity $\mathbf{v}_i(t)$ is then used for obtaining other velocity quantities, which we list next.

For the hydrodynamic paradigm, we convert the particle-level velocity data to hydrodynamic data through spatial averaging, which is done using bins. The symmetry of the flow in the experiment of Ref. [43] allows us to average over the particles within a rectangular bin that is narrow in the y direction but spans the entire width of the region of interest (ROI) in the ignorable x direction. This binning, denoted by brackets $\langle \rangle_{i,x}$, yields the hydrodynamic velocity

$$u_x(y, t) = \langle v_{ix}(\mathbf{r}_i, t) \rangle_{i,x}, \quad (3)$$

which is resolved in both y and t .

Another hydrodynamic measure, which is averaged over both y and t as well as x , is the global velocity of the entire dust cloud, $\mathbf{U} = (U_x, U_y) = \langle \mathbf{v}_i(\mathbf{r}_i, t) \rangle_{i,x,y}$. The overbar indicates an average over time, while the brackets $\langle \rangle_{i,x,y}$ indicate an average over all particles within the entire spatial extent, in both the x and y directions.

For a particle, the fluctuating component of its velocity is $\tilde{\mathbf{v}}_i(\mathbf{r}_i, t) = \mathbf{v}_i(\mathbf{r}_i, t) - \mathbf{U}$. Sometimes referred to as a particular velocity, $\tilde{\mathbf{v}}_i(\mathbf{r}_i, t)$ is essentially just the particle velocity in another inertial frame of reference. For the shear stress calculation, $\tilde{\mathbf{v}}_i$ will be an input, in Sec. II C.

The shear rate is the gradient of the hydrodynamic flow velocity $u_x(y, t)$:

$$\gamma(y, t) = \frac{\partial u_x(y, t)}{\partial y}. \quad (4)$$

This shear rate is resolved both in time t and the spatial direction y . Its time average is denoted $\overline{\gamma}(y)$. These measures of the shear rate will be used to obtain the viscosities using the nonequilibrium method.

C. Calculation of shear stress

To obtain the complex viscosity using either the equilibrium or nonequilibrium method, the shear stress P_{xy} is required. Often described as the off-diagonal element of the stress tensor, the shear stress for a 2D collection of particles is [59]

$$P_{xy}(t) = \frac{1}{A} \left[\sum_i m_d \tilde{v}_{ix} \tilde{v}_{iy} - \frac{1}{2} \sum_i \sum_{j \neq i} \frac{x_{ij} y_{ij}}{r_{ij}} \frac{\partial \Phi(r_{ij})}{\partial r_{ij}} \right]. \quad (5)$$

Here A is the area of the region to be analyzed, $\mathbf{r}_{ij}(t) = \mathbf{r}_i(t) - \mathbf{r}_j(t)$ is the distance between a pair of particles i and j , and $\mathbf{r}_{ij}(t)$ has an x -component $x_{ij}(t)$ and a y -component $y_{ij}(t)$. We note that this shear stress has the dimensions of a flux of momentum.

The inputs for calculating the shear stress include, for each particle i , the time series for the positions $(x_i(t), y_i(t))$ and velocities $(v_{ix}(\mathbf{r}_i, t), v_{iy}(\mathbf{r}_i, t))$. These can be measured directly in an experiment.

Also required in Eq. (5) are the interparticle potential energies $\Phi(r_{ij})$, for each pair of particles ij . When using

experimental data, it is necessary to calculate the potential energies assuming a model, which for a dusty plasma is typically the Yukawa electrical potential [18,24,25,41]:

$$\Phi(r_{ij}(t)) = \frac{Q^2}{4\pi\epsilon_0} \frac{e^{-r_{ij}(t)/\lambda_D}}{r_{ij}(t)}. \quad (6)$$

This model assumes that that electrons and ions provide isotropic shielding around a particle; it neglects the effects of ion wakes, ion-neutral collisions [81], and three-body interactions. The most commonly cited experiment for supporting the use of Eq. (6) is that of Konopka *et al.* [48].

Using Eq. (6), we can calculate the shear stress Eq. (5) with only an input of the measured particle positions and velocities:

$$P_{xy}(t) = \frac{m_d}{A} \left[\sum_i \tilde{v}_{ix} \tilde{v}_{iy} + \frac{a_{ws}^3 \omega_{pd}^2}{4} \sum_i \sum_{j \neq i} \times \frac{x_{ij} y_{ij}}{r_{ij}^2} e^{-r_{ij}/\lambda_D} \left(\frac{1}{r_{ij}} + \frac{1}{\lambda_D} \right) \right]. \quad (7)$$

In Eq. (7), area A is different for each method for obtaining the complex viscosity. For the *equilibrium* method, the shear stress is calculated for the entire analysis region, yielding a shear stress $P_{xy}(t)$ that is resolved only in time. For the *nonequilibrium* method, the ROI is split into bins. The shear stress is then obtained for each bin corresponding to a different value of y , so we obtain a shear stress $P_{xy}(y, t)$ that is resolved in both time and the y direction.

For a time series of infinite length, $P_{xy}(t)$ should have a time-average value of zero. However, we use a finite time series of data, which has some variations arising from the finite number of particles analyzed as well as from measurement error. Thus, the time average will, in general, have a small nonzero value, denoted $\overline{P_{xy}}$.

We subtract that time average value before calculating a viscosity using the shear stress data. This subtraction is done as

$$\tilde{P}_{xy}(y, t) = P_{xy}(y, t) - \overline{P_{xy}}(y) \quad (8)$$

for the nonequilibrium method, and

$$\tilde{P}_{xy}(t) = P_{xy}(t) - \overline{P_{xy}} \quad (9)$$

for the equilibrium method.

In calculating the shear stress using Eqs. (7)–(9), there is no limit to the value $r_{ij}(t)$ can take; however, in experiments and simulations, the particles are observed only in a finite observation region. Thus, the general practice is to truncate the potential at a maximum distance, termed a cutoff radius r_{cut} , when computing the shear stress [18,25,39,41,42].

III. CHARACTERIZING THE FREQUENCY-DEPENDENT COMPLEX VISCOSITY

Here, we review two standard methods for characterizing the complex viscosity of a fluid: *nonequilibrium* and *equilibrium*. The nonequilibrium method centers on the constitutive relation when there is a macroscopic gradient present. That gradient must be sustained by an external source. The equilibrium method, on the other hand, does not involve macroscopic gradients but instead extracts the complex viscosity from a

time series of microscopic fluctuations. A thermal equilibrium at temperature T_k is assumed for the equilibrium method, although we will actually apply the method under experimental conditions that only mimic thermal equilibrium.

To characterize the frequency dependence of the viscosity, we will use the symbol ω in both methods. However, we should note that ω has different meanings: In the nonequilibrium method, ω is prescribed by the experimenter who imposes an externally applied sinusoidal shear at that frequency, while in the equilibrium method ω is merely a Fourier-transform variable.

A. Nonequilibrium method

Transport coefficients are, in general, defined by a constitutive relation, i.e., a ratio of a flux and a gradient. Both the flux and the gradient that drives that flux are macroscopic quantities.

For the *static* viscosity, the constitutive relation is

$$\eta_{\text{neq}}^0(y) = -\frac{\overline{P_{xy}(y)}}{\overline{\gamma}(y)}, \quad (10)$$

where the subscript neq indicates the nonequilibrium method and the overbars again indicate a time-averaged quantity. The viscosity as defined by Eq. (10) is the ratio of a time-averaged flux and a time-averaged gradient. Here the relevant flux is the flux of momentum, the shear stress P_{xy} , and the corresponding gradient is the velocity gradient, the shear rate γ . As defined in Eqs. (7) and (4), respectively, these quantities on the right-hand side are functions of y . If this result $\eta_{\text{neq}}^0(y)$ is relatively uniform with respect to the nonignorable coordinate y , i.e., uniform over the gradient region as in Ref. [41], then we can spatially average to yield

$$\eta_{\text{neq}}^0 = \langle \eta_{\text{neq}}^0(y) \rangle_y, \quad (11)$$

which is the value of static viscosity that we will report for the nonequilibrium method.

To obtain the *complex* viscosity, which characterizes the time-dependent collective motion of particles, as explained by Ref. [54], we will calculate the viscosity as the ratio of two quantities in the *frequency domain*,

$$\eta_{\text{neq}}(y, \omega) = -\frac{P_{xy}(y, \omega)}{\gamma(y, \omega)}, \quad (12)$$

and not as the ratio of the two corresponding quantities $\overline{P_{xy}}(y, t)$ and $\overline{\gamma}(y, t)$ in the *time domain*. Nevertheless, we require the time-dependent expressions for $\overline{P_{xy}}(y, t)$ and $\overline{\gamma}(y, t)$ so we can Fourier-transform them to yield $P_{xy}(y, \omega)$ and $\gamma(y, \omega)$. These two frequency-dependent quantities have both real and imaginary parts, and we will retain both to yield the full complex viscosity.

In analogy with Eq. (11), we will spatially average $\eta_{\text{neq}}(y, \omega)$ over the ROI to yield

$$\eta_{\text{neq}}(\omega) = \langle \eta_{\text{neq}}(y, \omega) \rangle_y, \quad (13)$$

which is the value of complex viscosity that we will report for the nonequilibrium method

B. Equilibrium method

A more theoretical method of obtaining transport coefficients is the Green-Kubo relation. This calculation method is based on microscopic rather than macroscopic particle motions. It assumes thermal equilibrium conditions, without a macroscopic gradient, meaning without hydrodynamic shear. The Green-Kubo relation yields the viscosity as the time-integral of the autocorrelation function of the shear stress.

For the *static* viscosity, this relation is

$$\eta_{\text{eq}}^0 = \frac{A}{k_B T_k} \int_0^\infty C_\eta(t) dt, \quad (14)$$

where the subscript eq indicates the equilibrium method. The result is meaningful only if the integral converges, which requires [62] that the autocorrelation function $C_\eta(t)$ decay more rapidly than $1/t$.

The stress autocorrelation function (SACF) is

$$C_\eta(t) = \langle \widetilde{P_{xy}}(t) \widetilde{P_{xy}}(0) \rangle, \quad (15)$$

where $\widetilde{P_{xy}}(t)$ is defined in Eqs. (7) and (9).

To obtain the complex viscosity, the generalized Green-Kubo relation is [18,25,57,59,60]

$$\eta_{\text{eq}}(\omega) = \frac{A}{k_B T_k} \int_0^\infty C_\eta(t) e^{i\omega t} dt. \quad (16)$$

Equations (14)–(16) are intended for general use with liquids in the absence of macroscopic gradients. In principle, they can be used with many kinds of interparticle potential energies $\Phi(r_{ij})$ depending on the substance.

In practice, using the generalized Green-Kubo relation with an input of experimental data requires the use of a finite area as well as a finite time series, in obtaining the data for $C_\eta(t)$. We next describe the details of how we use the finite area and time.

The finite area for our equilibrium-method analysis is shown in Fig. 1(b). As in Ref. [39], we divide the camera's field of view into inner and outer rectangles. The inner rectangle is where the shear stress $P_{xy}(t)$ will be obtained, and this will require the potential energies within the inner rectangle. Those potential energies are the result not only of charges located within the inner rectangle, but outside it as well. Thus, potential energies $\Phi(r_{ij})$ will be calculated for a particle i within the inner rectangle, while particle j can be located anywhere in the inner or outer rectangles. The inner rectangle's dimensions are determined by our choice of the potential cutoff radius r_{cut} ; in particular, the width of the border between the rectangles is chosen to be equal to r_{cut} .

The finite time that is available when evaluating the integral in Eqs. (14) and (16) requires attention because, in theory, the integral is over an infinite time [18,25,39,42]. For simulation data, which have fluctuations that are nearly the same as for microscopic thermal fluctuations, one common practice is to evaluate the integral up to a maximum time that is the first zero crossing of the SACF [25,63]. Experimental data, however, can contain noise greater than nonthermal fluctuations [25,39,42], so the SACF oscillates noisily at long times. For choosing an integration limit in this situation, three approaches have been used in literature [25,39,42], and we will follow that of Ref. [42], which is based on the rms noise level

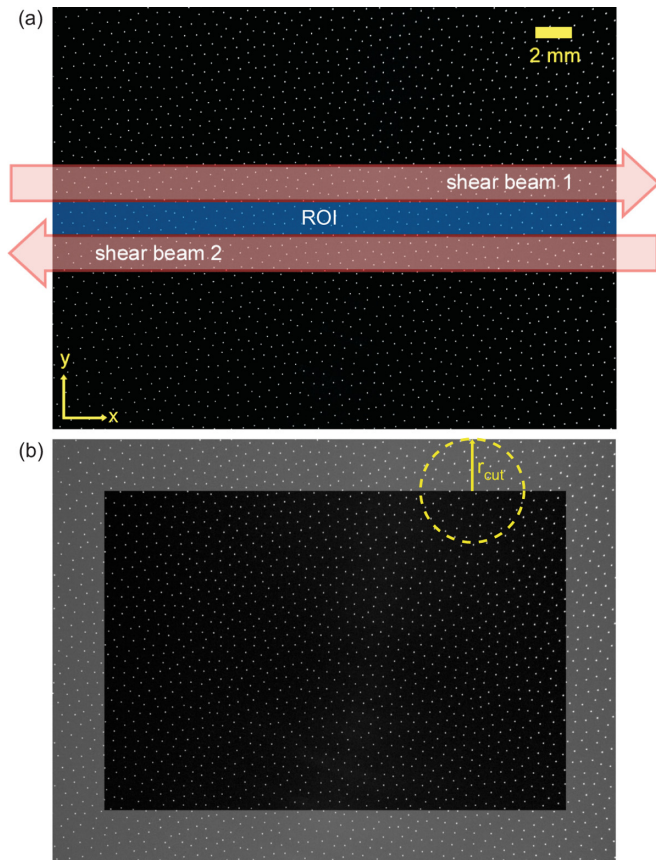


FIG. 1. Images from the top-view camera for liquid runs (a) with and (b) without an externally applied shear. The camera’s field of view of 24×32 mm, shown here, was centered in the dust particle cloud, which had a diameter of 64 mm. In (a), the broad arrows indicate the position and width of the two shear laser beams, which could be sinusoidally modulated at an externally controlled frequency ω . These beams were the source for the externally driven shear that made possible the use of the *nonequilibrium method* of analysis. The 2-mm gap between the shear beams was also the region of interest (ROI) for analyzing the hydrodynamic flow at the applied frequency ω . In (b), the analysis region for the *equilibrium method* was the inner rectangle defined by a gray border that has a thickness equal to r_{cut} . No shear beams were used for the runs analyzed with the equilibrium method. The position and thickness of the arrows in (a), as well as the width of the gray border in panel (b), are drawn to scale

for the SACF at long time. The integration limit for Eqs. (14) and (16) is thus taken as the time when the SACF has decayed to a value equal to the rms noise level, plus an increment of 1%.

IV. EXPERIMENT

In this paper, we carry out a different analysis of data from our previously reported experiment [43]. In Ref. [43], the data were analyzed to characterize a hydrodynamic phenomenon, the Stokes layer. Here, we analyze the data differently to characterize the complex viscosity $\eta(\omega)$.

The experiment is summarized below. A fuller description is provided in Ref. [43].

A. Apparatus

The experiment was performed in a partially ionized argon gas at 6 mTorr. The chamber included a horizontal lower electrode, which was driven by capacitively coupled radio frequency power, while all other surfaces were grounded.

After igniting the plasma, polymer particles were introduced. These were melamine formaldehyde microspheres [64] with a radius $r_d = 4.415 \mu\text{m}$ and a mass of $m_d = 5.45 \times 10^{-13}$ kg. A dispenser at the top of the chamber was agitated so particles fell into the plasma below. As they fell, they became charged and then levitated as a cloud at the upper edge of the sheath located above the horizontal lower electrode. By agitating the dispenser to an extent that allowed about 5700 particles to fall, it was assured that the cloud had only a single layer, which initially self-organized in a crystalline structure.

In the experiment of Ref. [43], the crystal was melted and liquid conditions were sustained, which is essential for our study of the viscoelastic properties of a liquid. To maintain these conditions, laser heating was used, with two laser beams swept in arcs so the radiation pressure force would give particles nearly random impulses of momentum.

The spatial uniformity of the heating was improved by sweeping the heating beams over the entire dust cloud [45]. This is different from relying on localized beams for heating as in Refs. [24,65,66].

To use the nonequilibrium method, a sinusoidal shear was added for certain runs. To apply a shear, a laser system was used, independent from the setup for laser heating. Two counterpropagating parallel laser beams were shaped as 2-mm-wide horizontal strips, as shown in Fig. 1(a). The radiation-pressure force from these two shear beams imparted a localized momentum to the particles within the beams. These beams were spaced with a 2-mm gap between the edges of the beams, so shear was applied externally within the beams but not within the gap. The flow pattern of dust particles, produced by the shear beams, was like that shown in Fig. 2 of Ref. [41]. As in Ref. [41], we aimed our camera downward at the center of the dust particle cloud, where the flow pattern was straight. Thus, we imaged a flow that mimicked the geometry of a traditional Couette flow, in which shear stress is applied by moving two planar boundaries of a sample liquid. In the experiment of Ref. [43], the boundaries of the sample were replaced by the two shear beams. More information regarding the width of the beams and the gap between them is provided in the Supplemental Material [67].

The shear-laser setup allowed applying shear either steadily as in Ref. [41] or with a modulation that was sinusoidal in time. This modulation was achieved by varying the intensity of the two laser beams sinusoidally, using a combination of a half-wave plate that was rotated at a controlled frequency, followed by a linear polarizer that was fixed in place.

As a key point, an effort was made to minimize shear thinning, which is the reduction in viscosity due to a large shear rate. To achieve a relatively low shear rate, we operated the shear beams at relatively low intensities. This choice was feasible because instead of relying on these shear beams for the additional purpose of heating and melting the crystal, which requires a great intensity, we used a separate pair of beams for

heating. To confirm that shear thinning was avoided, we note that the shear rate $\dot{\gamma}(y, t)$ in the experiment was always less than $0.15v_{\text{th}}/a_{\text{ws}}$. For comparison, the shear-thinning threshold for $\dot{\gamma}$ is $0.2v_{\text{th}}/a_{\text{ws}}$, as determined by Donkó *et al.* [68]. Thus, by operating below this threshold, shear thinning was minimized.

B. Procedure

Four kinds of runs were performed, all in a single day. *Crystal runs* were performed without any laser manipulation. *No-shear liquid runs* were done with the two heating laser beams, but without the shear laser beams. *Steady-shear runs* were carried out under liquid conditions, using not only the two heating beams but also the two shear beams, which were operated with a steady intensity. *Sinusoidal shear runs* were performed like the steady-shear runs but with a sinusoidal variation of the shear-beam intensities. Ten runs were performed with identical conditions for the sinusoidal shear runs. The other kinds of runs were each repeated four times, spaced throughout the day. The no-shear and shear runs provide our data for the equilibrium and nonequilibrium methods, respectively, of obtaining viscosity. The complete sequence of experimental runs is provided in the Supplemental Material [67].

The particle cloud was imaged from above, with illumination by a sheet of laser light. Using a top-view camera, videos were recorded. After waiting for steady conditions to be attained, the recordings were started. They lasted 42 seconds, which provided exactly an integer number of shear beam oscillations in each recording, for example, a recording included exactly 21 oscillations when the shear laser beams were modulated at 0.5 Hz. Among other details of the imaging, as described in Ref. [43], we mention a few of particular interest. The 24×32 mm field of view included about 2100 particles. The camera was operated at 50 or 100 frames per second for the crystal runs and other runs, respectively. Video images were analyzed using particle-tracking velocimetry [69,70], yielding particle positions $(x_i(t), y_i(t))$ and velocities $(v_{ix}(\mathbf{r}_i, t), v_{iy}(\mathbf{r}_i, t))$.

C. Dust cloud parameters

Many parameters describing the conditions within the camera's entire field of view were obtained in Ref. [43]. Besides the particle diameter and mass mentioned above, parameters used in our analysis include the following.

Several parameters are applicable to all runs, with or without laser manipulation. These include the areal mass density $\rho = (1.5 \pm 0.1) \times 10^{-6}$ kg/m², Wigner-Seitz radius $a_{\text{ws}} = 0.34 \pm 0.1$ mm, nominal 2D dust plasma frequency $\omega_{\text{pd}} = 81.0 \pm 0.4$ s⁻¹, screening length $\lambda_D = 0.49 \pm 0.1$ mm, and particle charge $Q = (17\,500 \pm 500) e$. These values remained steady during the experiment and their uncertainties are small enough to not change our conclusions, as discussed in the Supplemental Material [67].

For runs with laser heating manipulation, the kinetic temperature was $T_k = (2.0 \pm 0.1) \times 10^5$ K. This value, which is based on the mean-square velocity for the entire field-of-view of the camera, is a time average. (The rms fluctuations of the

kinetic temperature, partly due to the finite number of particles within the field of view, were 2×10^4 K.) The Coulomb coupling parameter was $\Gamma = 78 \pm 6$. As was noted in Ref. [43], the laser heating was sufficient to melt the crystal, and sustain liquid conditions. The measured temperature mentioned above exceeds the melting point [71] by a factor of 2.

D. Gas damping rate

A dusty plasma is a mixture of four components, including charged dust particles and a rarefied neutral gas. Among these components, only the dust particles are strongly coupled, so they can collectively behave like a liquid. This liquid occupies the same volume as the neutral gas. (We note that this condition, while common for dusty plasmas, is uncommon for other multiphase liquids, which do not commonly include a rarefied gas phase.) The gas exerts a friction force $m_d \nu_g v_i$ on a dust particle moving at velocity v_i , where ν_g is the gas damping rate. In the experiment we analyze [43], due to the use of a low gas pressure the damping rate had a small value $\nu_g = 0.97$ s⁻¹, which is $\ll \omega_{\text{pd}}$, indicating that the dust particle motion was underdamped [39,72].

Despite the underdamped condition, gas friction does have several dissipative effects on dust particle motion. One effect is cooling of the dust particle motion, which is necessary for the maintenance of a steady kinetic temperature, in the presence of constant energy inputs from ion flow and laser manipulation. Another effect is a complication in the viscoelastic combination of energy storage and energy dissipation. Gas friction alters this combination by providing additional energy dissipation, beyond that due to the microscopic breaking of bonds among neighboring dust particles. A quantification of gas friction's effect on viscoelastic behavior was reported in Ref. [18], where it was found that the effect was progressively more profound for a damping level $\nu_g/\omega_{\text{pd}} > 0.01$ in a three-dimensional simulation.

E. Thermal equilibrium conditions

Thermal equilibrium conditions actually do not prevail in laboratory dusty plasma experiments because the experiments always require external power supplies to sustain the plasma. Nevertheless, the random movements within a collection of particles in a dusty plasma can mimic those of a thermal equilibrium. Two criteria for assessing a thermal-equilibriumlike condition are often used for assessing numerical simulations of plasmas at a particle level. These criteria can also be used for dusty plasma experiments with particle-level data. The first criterion is that the velocity distribution function of the dust particles should be nearly Maxwellian. The second criterion is that the fluctuation level of the kinetic temperature, in a finite-size system, should be nearly the same as in a theoretical thermal equilibrium. Both these criteria were confirmed to be satisfied in earlier two-dimensional experiments [41,44]. We have also confirmed the criteria for the experiment we analyze [43], as we explain next.

To quantify how the velocity distribution is nearly Maxwellian, we fit the experimental velocity distribution to the theoretical Tsallis distribution [73,74], which is like a Maxwellian that is generalized to allow for enhanced tails.

Our fit yielded the parameter $q = 1.15 \pm 0.01$. This value is reasonably close to $q = 1$, which would correspond to a Maxwellian distribution.

The fluctuation level for the kinetic temperature was quantified by analyzing a time series of T_k for the 2100 particles within the camera's full field of view, using the method of Ref. [74]. We found that the experimental temperature fluctuation exceeded the theoretical canonical temperature fluctuation for a thermal equilibrium by a modest factor of 1.4. This factor is consistent with previous experiments that used laser-heating to produce two-dimensional liquids [41,44] like that of the experiment we analyze.

F. Comparison to previous dusty plasma experiments for obtaining the complex viscosity

Here, we compare our previous experiment [43] that we analyze here to some earlier dusty plasma experiments [24,25], where the complex viscosity was measured. There are many similarities, including the use of a two-dimensional layer of dust particles levitated above a lower horizontal electrode, and some type of laser manipulation.

For the equilibrium method of analysis, the experiment of Feng *et al.* [25] had no externally applied shear, so it resembled the no-shear liquid runs of the experiment we analyze. A major difference is that in Ref. [25] there were no additional runs with external shear. Additionally, we note that video recordings in Ref. [43] were of greater length.

For the nonequilibrium method, the experiment of Hartmann *et al.* [24] used a pair of counterpropagating laser beams to induce shear, which was sinusoidally modulated in time. We can point out three differences in the use of these counterpropagating beams, as compared to the experiment [43] that we analyze here. One difference is that the phase of one beam compared to the other was 180° in Ref. [24] but 0° in the experiment we analyze. Both setups are able to produce the time-dependent shear stress $P_{xy}(t)$ and shear rate $\gamma(t)$ needed for the nonequilibrium analysis. Two other differences, which are of greater importance, are described next.

First, and most importantly, the smaller shear rate γ used in Ref. [43] has the advantage of avoiding shear thinning, although it also has the disadvantage of reducing the signal strength, for the hydrodynamic velocity at the applied frequency. (This effect on the signal is greatest at high frequencies, so our analysis can only be done over a lower range of frequencies.) The greater shear rate used in the earlier experiment of Ref. [24] was necessary because no other laser manipulation was applied for melting, so the experimenters relied on shear-induced melting of the crystal.

Second, the shear beams in Ref. [43] were separated by a gap. This use of a gap promotes a greater uniformity of shear within the analyzed ROI, which is essentially the gap region. It also mimics a Couette flow, which has a gap between two boundaries where the shear is applied. In contrast, when the shear is driven by two laser beams that are more closely aligned, as in Ref. [24], the shear profile may be less uniform, and it may less closely mimic a uniform Couette flow.

V. OBTAINING THE COMPLEX VISCOSITY FROM THE EXPERIMENTAL DATA

The approach we use for analyzing experimental data is presented below. This presentation requires some detail, especially because our approach to the nonequilibrium method has not previously been used with experimental data.

A. Nonequilibrium method

Liquid runs *with* an externally applied shear were used to obtain the nonequilibrium viscosity $\eta_{\text{neq}}(\omega)$. For this method, the ROI was the gap between the shear laser beams, as shown in Fig. 1(a), where the shear was most uniform.

To convert the particle-level data to hydrodynamic data, we used binning as in Ref. [41,43]. Bins had a width of 0.50 mm in the y direction and a length that spanned the entire ROI in the x direction. Within each bin, we obtained time series for three hydrodynamic quantities: the hydrodynamic velocity $u_x(y, t)$ using Eq. (3), the shear rate $\gamma(y, t)$ using Eq. (4), and the shear stress $P_{xy}(y, t)$ using Eq. (7). The latter required a potential cutoff radius, which was chosen to be large enough, $6\lambda_D$, so the binary force due to a particle at the cutoff radius is $\approx 10^{-4}$ smaller compared to that due to a particle at a distance of λ_D .

As we explained in Sec. III A, we use a constitutive relation to obtain a nonequilibrium viscosity calculated as the ratio of a shear stress divided by a shear rate. These two quantities are both obtained with spatial resolution as a function of y by using data for shear stress and shear rate that have been binned. We then perform a simple average over all bins in the ROI, i.e., average over y , to yield a data point for the viscosity. (The averaging is possible due to the uniform shear region resulting from the Couette-flowlike configuration.) This process of binning and averaging after dividing the shear stress $P_{xy}(y, t)$ by the shear rate $\gamma(y, t)$ was carried out for the frequency-dependent complex viscosity $\eta_{\text{neq}}(\omega)$ using runs with sinusoidal modulation, as well as for the static viscosity η_{neq}^0 using runs with steady shear.

The main difference in the analysis for $\eta_{\text{neq}}(\omega)$, as compared to η_{neq}^0 , is that a discrete Fourier transform at the modulation frequency ω was applied to the time series data for shear rate and shear stress. For a time series $x(t)$, the discrete Fourier transform is calculated as

$$\frac{2\omega}{n\pi} \sum_{k=1}^N x(t_k) e^{i\omega t_k} \Delta t = R e^{i\phi}, \quad (17)$$

where t_k is the time, Δt is the step in time, n is the number of complete half periods in $x(t)$, and N is the largest integer closest to $2n\pi/\omega\Delta t$. This transform, for data within a bin corresponding to a given value of y , converted the time-series data into the frequency domain, yielding the amplitude R and phase ϕ , for both the frequency-dependent shear rate

$$\gamma(y, \omega) = R_\gamma(y, \omega) e^{i\phi_\gamma(y, \omega)}, \quad (18)$$

and the frequency-dependent shear stress

$$P_{xy}(y, \omega) = R_P(y, \omega) e^{i\phi_P(y, \omega)}. \quad (19)$$

The results of Eqs. (18) and (19) were then used as inputs for the constitutive relation Eq. (12), yielding the spatially

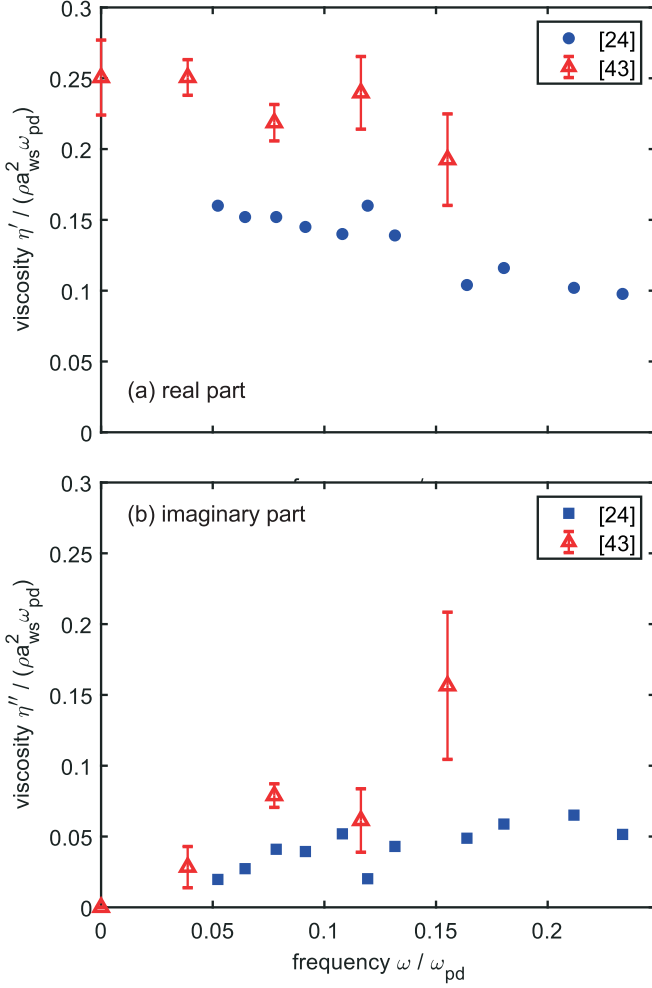


FIG. 2. Comparison of nonequilibrium experimental results. Data from the earlier experiment of Hartmann *et al.* [24] are plotted as solid symbols. Data points plotted as open triangles are from our analysis of the authors' recent experiment of Ref. [43]; each data point is the mean of the results for ten runs, with an error bar indicating the standard deviation of the mean. For normalization, viscosity is divided by $\rho a_{ws}^2 \omega_{pd}$ and frequency is divided by the nominal 2D dust plasma frequency ω_{pd} . While data from the two experiments generally have the same trends, there is a significant quantitative difference: Values for both $\eta'(\omega)$ and $\eta''(\omega)$ are smaller by at least a factor of 1.4 in the earlier experiment of Hartmann *et al.*, which may be attributed to shear thinning in the earlier experiment.

resolved complex viscosity

$$\eta_{\text{neq}}(y, \omega) = -\frac{R_P(y, \omega)}{R_Y(y, \omega)} e^{i(\phi_P(y, \omega) - \phi_Y(y, \omega))} \quad (20)$$

for each bin. The resulting values of $\eta_{\text{neq}}(y, \omega)$ for each bin were then averaged over y using Eq. (13) to yield $\eta_{\text{neq}}(\omega)$. We further averaged over all ten runs, for each modulation frequency ω .

Separately from our main results for $\eta_{\text{neq}}(\omega)$, obtained using the approach described above, we also obtained the static viscosity η_{neq}^0 . For this static viscosity, we used the same straightforward data-analysis approach as Haralson and Goree

[41] for analyzing data from experimental runs with steadily applied external shear.

B. Equilibrium method

Liquid runs *without* an externally applied shear were used to obtain the equilibrium viscosity $\eta_{\text{eq}}(\omega)$. For this method, the analysis region was the inner rectangle in Fig. 1(b). The border between the inner and outer rectangles had a breadth equal to r_{cut} , which was again chosen to be $6\lambda_D$.

The shear stress $P_{xy}(t)$ was calculated using Eq. (7), using particle-level data as the input. This shear stress was not spatially resolved, as it was calculated over the full analysis region. Using the time series of the shear stress as the input for Eq. (9), we obtained the fluctuating part of shear stress $\tilde{P}_{xy}(t)$, which in turn was used as the input for Eq. (15) to calculate the SACF, i.e., $C_\eta(t)$. Finally, this SACF, which had a finite duration, was the argument of the integral in the Green-Kubo calculations using Eq. (14) for the static viscosity η_{eq}^0 and Eq. (16) for the complex viscosity $\eta_{\text{eq}}(\omega)$.

The experimental SACF decayed not to zero, but to a noise floor that was 6% of $C_\eta(0)$. As in Ref. [42], this value guided us in selecting an upper time limit for the integrals in Eqs. (14) and (16). Following the prescription in Sec. III B, we chose the upper limit as the time when $C_\eta(t)$ had decayed within 7% of $C_\eta(0)$.

VI. RESULTS

Our chief results are the experimental complex viscosities $\eta(\omega)$. These results are presented in Figs. 2 and 3, as a function of frequency ω . We draw the reader's attention especially to the data for $\omega > 0$, which describe the viscoelastic properties of the 2D liquid. At $\omega = 0$ we also include data points, which correspond to the static viscosity η^0 .

A. Comparison to earlier nonequilibrium experiment

Results from the earlier nonequilibrium experiment of Hartmann *et al.* [24] can be compared directly to our nonequilibrium results. This comparison is presented in Fig. 2, using the same dimensionless units for the axes, so the use of particles with different mass and charge should not be a factor.

We find that our values of the frequency-dependent complex viscosity are generally greater than those of Hartmann *et al.* by a factor of at least 1.4. This difference appears for both the real and imaginary parts of the complex viscosity over the entire frequency range. The significance of these results is discussed in Sec. VII A.

B. Comparison of nonequilibrium versus equilibrium method

Comparing nonequilibrium versus equilibrium results, we find the same qualitative trends for both. As ω increases, the real part $\eta'(\omega)$ decreases; this decrease is expected because the dissipative physical effects described by $\eta'(\omega)$ require an extended time for microscopic rearrangements of particles. Likewise, as ω increases, the imaginary part $\eta''(\omega)$ increases, which is expected because the energy-storage effects associated with elasticity can survive only until the particles rearrange.

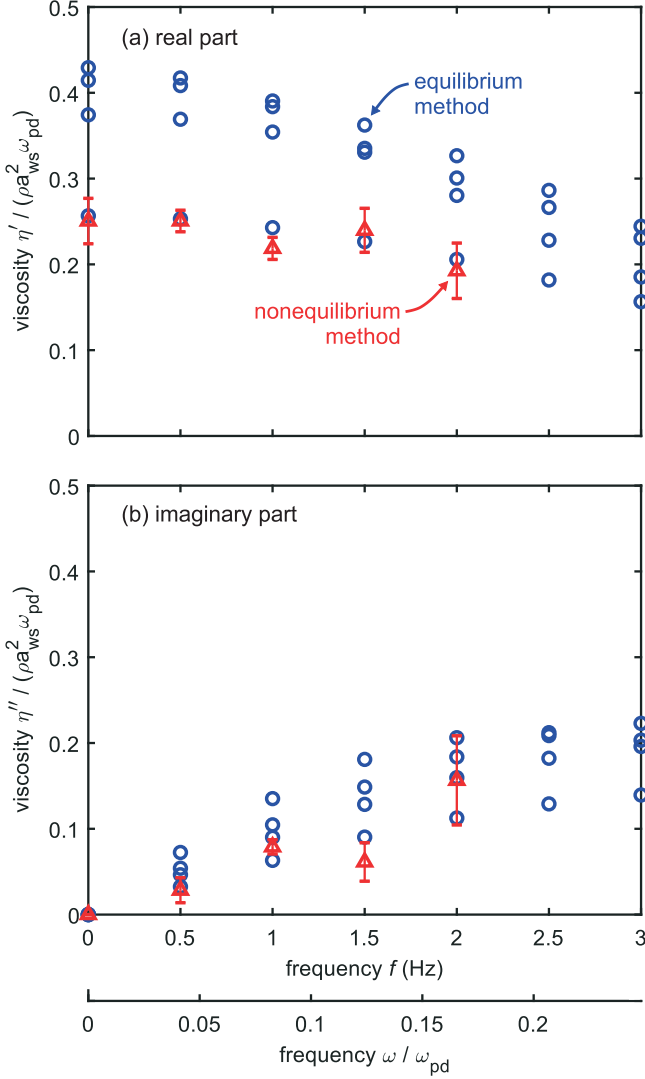


FIG. 3. Frequency-dependent complex viscosity: (a) real component $\eta'(\omega)$ and (b) imaginary component $\eta''(\omega)$. Circles represent equilibrium-method results obtained using Eqs. (15) and (16). Scatter of the four data points, each for one run, reflects the uncertainty. Triangles show nonequilibrium-method results, using Eqs. (12) and (13), as in Fig. 2. The static viscosity η^0 is indicated by the data points at $\omega = 0$. These results are our analysis of data from the experiment of Ref. [43].

Aside from this qualitative agreement of the two methods, we can also compare the results quantitatively. We find that the values of $\eta(\omega)$ obtained by the two methods differ slightly. The real part $\eta'_{\text{eq}}(\omega)$ is at least 31% greater (when averaged over four data points) as compared to the corresponding data point for the nonequilibrium method. The imaginary part $\eta''(\omega)$ is also greater for the equilibrium method, by at least 6%.

VII. DISCUSSION

A. Comparison to previous experiment

In Fig. 2, we compared results for $\eta(\omega)$ from two nonequilibrium experiments: Ref. [43], as analyzed in the current

paper, and the earlier experiment of Hartmann *et al.* [24]. We found a significant quantitative difference: Values of the frequency-dependent complex viscosity are generally greater than those of Hartmann *et al.* by a factor of at least 1.4.

Most likely, these differences arise from the different configurations of the experiments. As explained in Sec. IV F, the experiment of Hartmann *et al.* relied on the shear laser beams to also melt the crystal, which required a large shear. For the highest laser intensity, which was used for runs with nonzero frequencies, the zero-frequency shear was about $0.4v_{\text{th}}/a_{\text{ws}}$, as compared to $0.15v_{\text{th}}/a_{\text{ws}}$ for the experiment of Ref. [43] that we analyze. These values should be compared to the shear-thinning threshold (at zero frequency) of $0.2v_{\text{th}}/a_{\text{ws}}$, as reported by Donko *et al.* [68]. A diminishment of the complex viscosity due to high shear thinning is also demonstrated by the 2D simulations of Kovács *et al.* [61]. In their simulations, Kovács *et al.* found that high shear rates can significantly decrease the amplitudes of the real and imaginary parts of the complex viscosity for all frequencies. Thus, shear thinning could have been a factor in reducing the values of the zero-frequency viscosity η^0 in the experiment of Hartmann *et al.* Since Hartmann *et al.* used the same laser intensity to obtain the frequency-dependent viscosity $\eta(\omega)$, it seems possible that shear thinning may have occurred for those results as well. The experiment of Ref. [43], on the other hand, was designed specifically to minimize shear thinning, as discussed in Sec. IV A.

B. Interpretation of experimental results for nonzero frequency

In Fig. 3, there is a difference of at least 31% in the real component of the complex viscosity, for the equilibrium versus nonequilibrium methods. The physical cause for this difference is not yet known, but we can discuss several possibilities.

One possibility is shear thinning, but an effort was made to minimize this effect in the experiment, as explained in Sec. IV A. A second possibility, gas friction, is not expected to have a significant effect when the damping rate is low [18,39,61,72], which is the case in the experiment. A third possibility could be the finite duration of the experimental time series, as the Green-Kubo relations, Eqs. (14) and (16), require integrating over an infinite time. The finite duration of the experimental time series was found not to be a likely source of the increased value of the complex viscosity, according to a test we performed, as described in the Supplemental Material [67].

Three other possible explanations for the difference were mentioned previously, by Haralson and Goree [42], who reported a similar difference for the static shear viscosity. Their explanations involve dimensionality, interactions between particles, and thermal properties of the liquid-like dust cloud, as we elaborate below.

Low dimensionality could be a factor. The dust particles did not fill a three-dimensional volume but instead were mainly constrained to move on a horizontal plane. It remains an unresolved physics question whether transport coefficients like viscosity are strictly valid in two dimensions [62,75–78].

Interactions of particles in the experiment may be more complicated than the binary Yukawa interaction that we as-

sumed in calculating the shear stress. One issue is that a binary Yukawa interaction neglects ion wake effects [79,80] as well as possible long-distance deviations from the Yukawa potential [81]. This should not be a factor because the same potential was used for both methods when calculating the complex viscosity. Another issue is the binary interaction approximation, i.e., the omission of three-body interactions, in calculating the complex viscosity. Indications of three-body interactions have been reported by other experimenters [82]. It is possible that three-body interactions might play a different role in momentum transfer, in the presence of macroscopic shear, as compared to the microscopic fluctuating shear that enters the underlying theory for the equilibrium method.

Thermal properties of the liquidlike dust cloud in the experiment are in fact more complicated than a theoretical thermal equilibrium. As mentioned in Ref. [42], the liquidlike collection of dust particles in the experiment only *mimicked* thermal equilibrium in terms of the velocity distribution function and temperature fluctuations. The dust cloud was actually nonequilibrium, as almost all laboratory plasmas are, because it relied on energy inputs from external power supplies and lasers while there was a constant energy loss to the neutral gas. The Green-Kubo relations, Eqs. (14) and (16), are intended for liquids under thermal equilibrium conditions.

C. Interpretation of experimental results for zero frequency

While we have directed most of our attention to our results for nonzero frequency, we also obtained a result for zero frequency, i.e., static viscosity. This result appears on the far left of Fig. 3. Comparing the results from both methods, we find that the static viscosity η^0 was about 40% greater for the equilibrium method as compared to the nonequilibrium method.

This outcome demonstrates a reproducibility of the earlier result of Haralson and Goree [42]. In that paper, an experiment was reported that used largely the same instrumentation as in Ref. [43]. The difference was found to be about 60%, for η^0 obtained by the equilibrium versus nonequilibrium methods.

D. Comparison to previous simulations

Three simulation approaches were used by Donkó *et al.* [18] to obtain the complex viscosity $\eta(\omega)$. One was a nonequilibrium simulation, using an externally applied shear, with the complex viscosity calculated as in Eqs. (12) and (13). This simulation ignored gas friction. The other simulations used equilibrium conditions, without macroscopic shear, and the complex viscosity was calculated as in Eq. (16). These two equilibrium simulations differed in the description of gas friction, which was included in only one of them.

The results of these simulations revealed the same trends as seen in our experimental results for the variation of complex viscosity with frequency. However, unlike the experiment we analyze, these simulations yielded a close agreement of equilibrium and nonequilibrium results. The agreement was within a few percent, without a systematic tendency for one method to yield a greater value than the other.

While we cannot fully reconcile our experimental results with the simulation results of Donkó *et al.*, we can note six fundamental differences between experiment and simulation.

First, the experiment in Ref. [43] was two-dimensional while the simulation of Donkó *et al.* was three-dimensional. Second, the interaction potential was assumed to be a binary Yukawa interaction for the simulations of Donkó *et al.*, unlike the experiment, where three-body interactions are possible. Third, the maintenance of a nearly steady temperature was different in the experiment and simulation in the absence of shear. Fourth, the methods of applying shear in the experiment and the simulation were different for the nonequilibrium method. Fifth, the boundaries were different in the experiment and simulation. Sixth, gas friction played a significant role in the experiment for both the equilibrium and nonequilibrium methods, but was absent for both methods in the simulation [18]. These differences are further explained in the Supplemental Material [67].

VIII. CONCLUSION

We studied the viscoelastic properties of a two-dimensional dusty plasma, which was in a liquid phase that was sustained by laser heating. Using data recorded in the same experiment [43], two methods for calculating the complex viscosity $\eta(\omega)$ were compared. The nonequilibrium method is based on the constitutive relation, and the equilibrium method is based on the generalized Green-Kubo relation.

As the frequency varied, the complex viscosity obtained by these two methods exhibits the same trends: the real part $\eta'(\omega)$ decreases with ω while the imaginary part $\eta''(\omega)$ increases with ω . These trends are expected because, for a viscoelastic substance, the dissipative effects measured by $\eta'(\omega)$ should be strongest on long timescales, while the energy-storage effects measured by $\eta''(\omega)$ should be greatest at short timescales.

We compared our $\eta(\omega)$ from our nonequilibrium-method analysis of the experiment of Ref. [43] to those of an earlier experiment performed by Hartmann *et al.* [24]. While the trends were the same [$\eta'(\omega)$ decreasing with ω but $\eta''(\omega)$ increasing with ω], there were substantial quantitative differences. We note that, unlike the earlier experiment of Hartmann *et al.*, the recent experiment [43] that we analyze was designed to minimize shear thinning, and this may account for the difference.

We also compared the two methods for calculating $\eta(\omega)$ and found that, for the real part $\eta'(\omega)$, the equilibrium method yielded values that were slightly larger, by at least 31%, than did the nonequilibrium method. The same was true for the imaginary part $\eta''(\omega)$, although the percentage difference was generally not as great. The underlying reason for this difference has not been identified yet, but some possibilities were discussed in Sec. VII B. We also note that compared to this outcome for a 2D experiment, there was little difference in the results of the equilibrium and nonequilibrium methods in previous 3D simulations [18].

Separately, we note that our results for zero frequency shear viscosity, i.e., the static shear viscosity η^0 , allow us to confirm the reproducibility of the experimental results of Ref. [42].

ACKNOWLEDGMENTS

This work was supported by U.S. Department of Energy, No. DE-SC0014566, the Army Research Office,

No. W911NF-18-1-0240, and NASA-JPL Subcontracts No. 1573629 and No. 1663801. We thank Z. Haralson, A. Kananovich, B. Liu, and our MURI team collaborators

for helpful discussions. We thank Vitaliy Zhuravlyov for technical assistance. We thank P. Hartmann for providing experiment data in Fig. 2.

-
- [1] N. W. Tschoegl, *The Phenomenological Theory of Linear Viscoelastic Behavior*, 1st ed. (Springer-Verlag, Berlin, 1989).
- [2] S. Ichimaru, *Rev. Mod. Phys.* **54**, 1017 (1982).
- [3] S. Ichimaru and S. Tanaka, *Phys. Rev. Lett.* **56**, 2815 (1986).
- [4] S. Ichimaru, H. Iyetomi, and S. Tanaka, *Phys. Rep.* **149**, 91 (1987).
- [5] P. K. Kaw and A. Sen, *Phys. Plasmas* **5**, 3552 (1998).
- [6] M. S. Murillo, *Phys. Plasmas* **7**, 33 (2000).
- [7] B. S. Xie and M. Y. Yu, *Phys. Rev. E* **62**, 8501 (2000).
- [8] D. Banerjee, J. S. Mylavarapu, and N. Chakrabarti, *Phys. Plasmas* **17**, 113708 (2010).
- [9] B. M. Veerasha, S. K. Tiwari, A. Sen, P. K. Kaw, and A. Das, *Phys. Rev. E* **81**, 036407 (2010).
- [10] S. Ghosh, M. R. Gupta, N. Chakrabarti, and M. Chaudhuri, *Phys. Rev. E* **83**, 066406 (2011).
- [11] R. P. Prajapati and R. K. Chhajlani, *Astrophys. Space Sci.* **344**, 371 (2013).
- [12] J. S. Dhiman and R. Sharma, *Phys. Scr.* **89**, 125001 (2014).
- [13] A. Gupta, R. Ganesh, and A. Joy, *Phys. Plasmas* **21**, 073707 (2014).
- [14] A. Diaw and M. S. Murillo, *Phys. Rev. E* **92**, 013107 (2015).
- [15] Y. Wang, X. Guo, Y. Lu, and X. Wang, *Phys. Lett. A* **380**, 215 (2016).
- [16] Y. Ghai, N. S. Saini, and M. Singh, *IEEE Trans. Plasma Sci.* **46**, 825 (2018).
- [17] Y. Wang, *AIP Adv.* **9**, 125216 (2019).
- [18] Z. Donkó, J. Goree, and P. Hartmann, *Phys. Rev. E* **81**, 056404 (2010).
- [19] J. Goree, Z. Donkó, and P. Hartmann, *Phys. Rev. E* **85**, 066401 (2012).
- [20] J. Pramanik, G. Prasad, A. Sen, and P. K. Kaw, *Phys. Rev. Lett.* **88**, 175001 (2002).
- [21] S. Ratynskaia, K. Rypdal, C. Knapik, S. Khrapak, A. V. Milovanov, A. Ivlev, J. J. Rasmussen, and G. E. Morfill, *Phys. Rev. Lett.* **96**, 105010 (2006).
- [22] C. L. Chan and L. I, *Phys. Rev. Lett.* **98**, 105002 (2007).
- [23] P. Bandyopadhyay, G. Prasad, A. Sen, and P. K. Kaw, *Phys. Lett. A* **372**, 5467 (2008).
- [24] P. Hartmann, M. C. Sándor, A. Kovács, and Z. Donkó, *Phys. Rev. E* **84**, 016404 (2011).
- [25] Y. Feng, J. Goree, and B. Liu, *Phys. Rev. E* **85**, 066402 (2012).
- [26] J. J. Bollinger, D. J. Wineland, and D. H. Dubin, *Phys. Plasmas* **1**, 1403 (1994).
- [27] M. Rosenberg and P. K. Shukla, *Phys. Scr.* **83**, 015503 (2011).
- [28] M. Lyon and S. L. Rolston, *Rep. Prog. Phys.* **80**, 017001 (2017).
- [29] J. Goree, B. Liu, and Y. Feng, *Plasma Phys. Control. Fusion* **55**, 124004 (2013).
- [30] J. H. Chu and L. I, *Phys. Rev. Lett.* **72**, 4009 (1994).
- [31] Y. Hayashi and K. Tachibana, *Jpn. J. Appl. Phys.* **33**, L804 (1994).
- [32] H. Thomas, G. E. Morfill, V. Demmel, J. Goree, B. Feuerbacher, and D. Möhlmann, *Phys. Rev. Lett.* **73**, 652 (1994).
- [33] H. Totsuji, C. Totsuji, and K. Tsuruta, *Phys. Rev. E* **64**, 066402 (2001).
- [34] A. Melzer, *Physics of Dusty Plasmas: An Introduction*, Lecture Notes in Physics, Vol. 962 (Springer, Heidelberg, 2017).
- [35] L. Couëdel, V. Nosenko, S. K. Zhdanov, A. V. Ivlev, H. M. Thomas, and G. E. Morfill, *Phys. Rev. Lett.* **103**, 215001 (2009).
- [36] P. Hartmann, A. Douglass, J. C. Reyes, L. S. Matthews, T. W. Hyde, A. Kovács, and Z. Donkó, *Phys. Rev. Lett.* **105**, 115004 (2010).
- [37] P. Hartmann, A. Z. Kovács, A. M. Douglass, J. C. Reyes, L. S. Matthews, and T. W. Hyde, *Phys. Rev. Lett.* **113**, 025002 (2014).
- [38] B. Liu and J. Goree, *Phys. Rev. E* **75**, 016405 (2007).
- [39] Y. Feng, J. Goree, B. Liu, and E. G. D. Cohen, *Phys. Rev. E* **84**, 046412 (2011).
- [40] V. Nosenko, A. V. Ivlev, and G. E. Morfill, *Phys. Rev. Lett.* **108**, 135005 (2012).
- [41] Z. Haralson and J. Goree, *Phys. Plasmas* **23**, 093703 (2016).
- [42] Z. Haralson and J. Goree, *Phys. Rev. Lett.* **118**, 195001 (2017).
- [43] J. Berumen and J. Goree, *Phys. Rev. E* **104**, 035208 (2021).
- [44] V. Nosenko, J. Goree, and A. Piel, *Phys. Plasmas* **13**, 032106 (2006).
- [45] Z. Haralson and J. Goree, *IEEE Trans. Plasma Sci.* **44**, 549 (2016).
- [46] M. M. Abbas, P. D. Craven, J. F. Spann, W. K. Witherow, E. A. West, D. L. Gallagher, M. L. Adrian, G. J. Fishman, D. Tanosic, A. LeClair *et al.*, *J. Geophys. Res.* **108**, 1229 (2003).
- [47] B. Liu, J. Goree, V. Nosenko, and L. Boufendi, *Phys. Plasmas* **10**, 9 (2003).
- [48] U. Konopka, G. E. Morfill, and L. Ratke, *Phys. Rev. Lett.* **84**, 891 (2000).
- [49] C. S. Wong, J. Goree, Z. Haralson, and B. Liu, *Nat. Phys.* **14**, 21 (2017).
- [50] A. Gemant, *Trans. Faraday Soc.* **31**, 1582 (1935).
- [51] J. D. Ferry, *Viscoelastic Properties of Polymers*, 3rd ed. (John Wiley & Sons, New York, 1980).
- [52] R. B. Bird and A. J. Giacomin, *Rheol. Acta* **51**, 481 (2012).
- [53] A. A. Collyer, *Techniques in Rheological Measurement*, 1st ed. (Springer Netherlands, Dordrecht, 1993).
- [54] D. J. Evans and G. P. Morris, *Statistical Mechanics of Nonequilibrium Liquids*, 1st ed. (Academic Press, London, 1990).
- [55] J. D. Menczel and R. B. Prime, *Thermal Properties of Polymers: Fundamentals and Applications*, 1st ed. (John Wiley & Sons, Hoboken, 2009).
- [56] K. P. Menard and N. R. Menard, Dynamic mechanical analysis in the analysis of polymers and rubbers, in *Encyclopedia of Polymer Science and Technology* (John Wiley & Sons, 2015).
- [57] R. Zwanzig and R. D. Mountain, *J. Chem. Phys.* **43**, 4464 (1965).
- [58] R. Zwanzig, *Annu. Rev. Phys. Chem.* **16**, 67 (1935).
- [59] P. Hansen and I. R. McDonald, *Theory of Simple Liquids*, 2nd ed. (Elsevier Academic, Amsterdam, 1986).

- [60] R. Zangi and L. J. Kaufman, *Phys. Rev. E* **75**, 051501 (2007).
- [61] A. Z. Kovács, P. Hartmann, and Z. Donkó, *Phys. Plasmas* **22**, 103705 (2015).
- [62] Z. Donkó, J. Goree, P. Hartmann, and B. Liu, *Phys. Rev. E* **79**, 026401 (2009).
- [63] Y. Zhang, A. Otani, and E. J. Maginn, *J. Chem. Theory Comput.* **11**, 3537 (2015).
- [64] Melamine-formaldehyde microspheres manufactured by micro-particles GmbH, Berlin, Germany, <http://www.microparticles.de/>.
- [65] V. Nosenko and J. Goree, *Phys. Rev. Lett.* **93**, 155004 (2004).
- [66] Y. Feng, J. Goree, and B. Liu, *Phys. Rev. Lett.* **109**, 185002 (2012).
- [67] See Supplemental Material at <http://link.aps.org/supplemental/10.1103/PhysRevE.105.015209> for additional information regarding the experiment, an error analysis of the complex viscosity calculations, and an in depth comparison between experiment and simulation.
- [68] Z. Donkó, J. Goree, P. Hartmann, and K. Kutasi, *Phys. Rev. Lett.* **96**, 145003 (2006).
- [69] Y. Feng, J. Goree, and B. Liu, *Rev. Sci. Instrum.* **78**, 053704 (2007).
- [70] Y. Feng, J. Goree, and B. Liu, *Rev. Sci. Instrum.* **82**, 053707 (2011).
- [71] P. Hartmann, G. J. Kalman, Z. Donkó, and K. Kutasi, *Phys. Rev. E* **72**, 026409 (2005).
- [72] Y. Feng, J. Goree, and B. Liu, *Phys. Plasmas* **18**, 057301 (2011).
- [73] C. Tsallis, S. V. F. Levy, A. M. C. Souza, and R. Maynard, *Phys. Rev. Lett.* **75**, 3589 (1995).
- [74] B. Liu, J. Goree, and Y. Feng, *Phys. Rev. E* **78**, 046403 (2008).
- [75] B. J. Alder and T. E. Wainwright, *Phys. Rev. A* **1**, 18 (1970).
- [76] M. H. Ernst, E. H. Hauge, and J. M. J. van Leeuwen, *Phys. Rev. Lett.* **25**, 1254 (1970).
- [77] J. R. Dorfman and E. G. D. Cohen, *Phys. Rev. A* **6**, 776 (1972).
- [78] Y. Pomeau and P. Résibois, *Phys. Rep.* **19**, 63 (1975).
- [79] A. Piel, O. Arp, D. Block, I. Pilch, T. Trottenberg, S. Käding, A. Melzer, H. Baumgartner, C. Henning, and M. Bonitz, *Plasma Phys. Control. Fusion* **50**, 124003 (2008).
- [80] D. Block, J. Carstensen, P. Ludwig, W. J. Miloch, F. Greiner, A. Piel, M. Bonitz, and A. Melzer, *Contrib. Plasma Phys.* **52**, 804 (2012).
- [81] R. Kompaneets, U. Konopka, A. V. Ivlev, V. Tsytovich, and G. Morfill, *Phys. Plasmas* **14**, 052108 (2007).
- [82] O. S. Vaulina, O. F. Petrov, V. E. Fortov, A. V. Chernyshev, A. V. Gavrikov, and O. A. Shakhova, *Phys. Rev. Lett.* **93**, 035004 (2004).